

# A method for reducing specular reflections in Mueller matrix imaging

IAGO PARDO,<sup>1,2</sup> SUBIAO BIAN,<sup>1,2</sup> ESTHER PASCUAL<sup>1,2</sup> AND ORIOL ARTEAGA<sup>1,2,\*</sup>

<sup>1</sup> Dep. Física Aplicada, PLAT group, Universitat de Barcelona, IN2UB Barcelona 08028, Spain

<sup>2</sup> Institute of Nanoscience and Nanotechnology (IN2UB), Universitat de Barcelona, Barcelona 08028, Spain

\*oarteaga@ub.edu

**Abstract:** Mueller matrix polarimetry has emerged as a powerful tool for non-destructive optical analysis of biological tissues and bioorganic materials, offering detailed insights into polarization-specific properties such as diattenuation, retardance, and depolarization. However, the accurate application of Mueller matrix polarimetry in biological media is often hindered by specular reflections, which obscure signals from deeper tissue layers and degrade the sample visualization and the polarimetric data quality. Existing methods to minimize specular reflection have limitations, especially in clinical or in-vivo settings where sample positioning is constrained. Here, we introduce a new approach for avoiding or reducing specular highlights without having to reduce light's intensity. By using near-cross-polarization states between the polarization state state generator and analyzer, we demonstrate that one can obtain an enhanced visualization of tissue structures, reduce the appearance of specular reflections and improve polarimetric contrast.

© 2025 Optica Publishing Group

## 1. Introduction

Mueller matrix (MM) polarimetry has rapidly evolved as a crucial tool for the optical analysis of biological systems and bio-organic materials, providing non-destructive access to the microstructural and polarization-specific characteristics of complex tissues [1–8]. By capturing full polarimetric information, MM polarimetry allows for detailed measurements of properties such as diattenuation, retardance, and depolarization, essential in fields ranging from biomedical diagnostics to materials science [9, 10]. A significant advantage of MM polarimetry lies in its adaptability; it can operate in both transmission and reflection modes, making it versatile for a broad array of applications [11], including examining layered tissues, monitoring structural changes, and identifying biomolecular alignments in healthy and pathological tissues [12, 13].

Despite its many advantages, MM polarimetry faces notable challenges when applied in vivo to scattering media and complex biological tissues, primarily due to the effects of specular reflections. Specular reflections, resulting from direct surface reflections, sometimes can obscure the polarimetric signals originating from deeper within the tissue [14]. Specular reflections often produce strong co-polarized components that saturate the detector, making it challenging to isolate signals related to subsurface tissue features, which generally exhibit reduced polarization due to scattering. When unaddressed, specular reflections degrade the quality of the polarimetric data, potentially leading to misinterpretations of tissue properties, particularly when investigating surface and near-surface structures.

Conventional methods to mitigate specular reflection in MM polarimetry and other biomedical imaging techniques involve orienting the sample at an angle to deflect specular reflections away from the detector's path [6, 15]. Additional approaches include reducing the intensity of the light source to minimize reflective contributions or employing image processing software to exclude saturated areas from measurements [16]. Advanced algorithms have also been proposed for this purpose [17–19]. Although somewhat effective, these methods have limitations. Tilting the sample, for example, is not always feasible, especially in clinical or in-vivo applications where

sample positioning is constrained and the investigated tissues are not flat and often immersed in fluids (blood, cerebrospinal fluid, etc) [20, 21]. Lowering the light intensity, while reducing the impact of specular reflection, can also lead to more noisy measurements, limiting the overall information that can be obtained about the sample and potentially masking critical features. These challenges highlight the need for an approach that effectively minimizes specular reflection without compromising the illumination conditions.

In this work, we propose a method that exploits differences in polarization state to effectively reduce the impact of specular reflections, thus enhancing image quality and measurement accuracy in MM polarimetry. Our approach is based on tailoring the polarization state generation and analysis processes, using sets of angles that favor near-cross-polarized states. By doing so, we selectively suppress or reduce specular reflections that retain high degrees of polarization while preserving light coming from depolarizing tissue structures. Notably, many biomedical imaging methods, already use crossed-polarizers to reduce specular reflections [22, 23], particularly in dermatological applications [24, 25]. Our method advances this concept by making it compatible with full MM polarimetry. Our method enables the use of higher light intensities, thereby improving polarimetric contrast and extending the dynamic range of measurements. This results in more accurate visualization of biological tissues and their polarimetric properties, unlocking valuable insights into complex biological samples.

To demonstrate the efficacy of this method, we implement it in an MM imaging system using two rotating compensators. However, the underlying strategy is adaptable and can be applied to systems employing liquid crystals or other polarization control devices, ensuring broad applicability across different MM polarimetry setups.

## 2. Theoretical framework

A typical MM system, utilizing a two-rotating-compensator configuration, consists of a Polarization State Generator (PSG) and a Polarization State Analyzer (PSA). The PSG produces at least four independent polarization states, which interact with the sample. The PSA then analyzes the resulting polarization states by measuring their projections onto at least four other linearly independent states. Both the PSG and PSA are composed of a polarizer and a rotating compensator.

In a MM polarimetry experiment, the Stokes vector detected is expressed as [26]:

$$\mathbf{S}_{\text{out}} = \mathbf{M}_{PSA} \mathbf{M} \mathbf{M}_{PSG} \mathbf{S}_{\text{in}}, \quad (1)$$

where  $\mathbf{M}$ ,  $\mathbf{M}_{PSA}$  and  $\mathbf{M}_{PSG}$  are respectively the Mueller matrices of the sample, the PSA and the PSG.

The detector used in most imaging systems is only sensitive to the first component of the Stokes vector  $I$ , and because of this, only the first row of  $\mathbf{M}_{PSA}$  and the first column of  $\mathbf{M}_{PSG}$  will affect the intensity obtained. Therefore we can write the previous expression as:

$$I_k = \begin{pmatrix} a_{k,0} & a_{k,1} & a_{k,2} & a_{k,3} \end{pmatrix} \begin{pmatrix} m_{00} & m_{01} & m_{02} & m_{03} \\ m_{10} & m_{11} & m_{12} & m_{13} \\ m_{20} & m_{21} & m_{22} & m_{23} \\ m_{30} & m_{31} & m_{32} & m_{33} \end{pmatrix} \begin{pmatrix} g_{k,0} \\ g_{k,1} \\ g_{k,2} \\ g_{k,3} \end{pmatrix} = \mathbf{A}_k^T \mathbf{M} \mathbf{G}_k, \quad (2)$$

where  $k$  refers to the  $k^{th}$  intensity measurement made at the detector.

In a system based on two rotating compensators, the Mueller matrices of PSA and PSG in Eq. (1) are

$$\mathbf{M}_{PSG} = \mathbf{R}(-\theta_0) \mathbf{M}_{LR_0} \mathbf{R}(\theta_0) \mathbf{P}_0, \quad (3)$$

84

$$\mathbf{M}_{PSA} = \mathbf{P}_1 \mathbf{R}(\theta_1) \mathbf{M}_{LR1} \mathbf{R}(-\theta_1), \quad (4)$$

85 where  $\mathbf{P}$  and  $\mathbf{R}$  are the Mueller matrices of a linear polarizer and the usual rotation matrix,  
 86 respectively and  $\mathbf{M}_{LR}$  is the MM of a compensator with linear retardance  $\delta$ .  $\theta_0$  and  $\theta_1$  are the  
 87 orientation angles of the compensator. Therefore the PSG and PSA can be expressed as [27]:

$$\mathbf{G} = \begin{pmatrix} 1 \\ \cos(2\theta_0)^2 + \cos(\delta_0) \sin(2\theta_0)^2 \\ \cos(2\theta_0) \sin(2\theta_0) (1 - \cos(\delta_0)) \\ \sin(\delta_0) \sin(2\theta_0) \end{pmatrix}, \quad \mathbf{A} = \begin{pmatrix} 1 \\ -(\cos(2\theta_1)^2 + \cos(\delta_1) \sin(2\theta_1)^2) \\ -\cos(2\theta_1) \sin(2\theta_1) (1 - \cos(\delta_1)) \\ \sin(\delta_1) \sin(2\theta_1) \end{pmatrix}. \quad (5)$$

88 To obtain  $N$  intensity measurements, there are two possible operating modes for rotating  
 89 compensator systems: continuous and discrete rotation. In the discrete mode, the compensators  
 90 are positioned at predetermined angles, allowing full flexibility in selecting the specific angles.  
 91 The method of this work utilizes the discrete mode. One key advantage of the discrete mode for  
 92 imaging applications is its independence from the detector's integration time and the compensators'  
 93 rotation speed. This means that, in cases where the signal is low, the camera's exposure time  
 94 can be increased without affecting data processing. It is worth noting that maintaining linearity  
 95 requires using the same exposure for all acquisition angles. If a particular angle causes substantial  
 96 saturation in the detector, the light source intensity or exposure time must be adjusted for all other  
 97 angles, sometimes compromising the measurement quality.

98 Using linear algebra properties, it is possible to rewrite Eq. (2) as a scalar product between  
 99 two vectors

$$\mathbf{I}_k = \mathbf{W}_k^T \vec{\mathbf{M}}, \quad (6)$$

100 where  $\mathbf{W}_k = \mathbf{A}_k^T \otimes \mathbf{G}_k$  and  $\vec{\mathbf{M}}$  is the 16-component Mueller vector.

101 The polarimetric data analysis will consist of solving Eq. 6 for the Mueller vector. If the  
 102 measurements consist of  $N$  intensity measurements, we can rewrite Eq. 6 as

$$\mathbf{I} = \mathbf{W} \vec{\mathbf{M}}, \quad (7)$$

103 where  $\mathbf{I}$  is the intensity vector over all the measurements and  $\mathbf{W}$  is a matrix of dimension  $N \times 16$   
 104 that relates the measured intensities with the MM elements. So, the MM of the sample can be  
 105 extracted as [26],

$$\vec{\mathbf{M}} = (\mathbf{W} \mathbf{W}^T)^{-1} \mathbf{W} \mathbf{I} = \mathbf{W}^+ \mathbf{I}, \quad (8)$$

106 where  $\mathbf{W}^+$  is the pseudo-inverse of  $\mathbf{W}$ , which gives the least squares estimate of the inverse.

107 In a transmission experiment, if the sample does not alter the polarization of light, the intensity  
 108 in Eq. (7) is maximized when the Stokes vectors associated with the PSA and PSG are equal  
 109 ( $a_{k,j} = g_{k,j}$  for  $j = 0, 1, 2, 3$ ) and minimized when they are orthogonal ( $a_{k,j} = -g_{k,j}$  for  
 110  $j = 1, 2, 3$ ). In a backscattering configuration, the specular reflection has an associated MM  
 111  $\mathbf{M} = \text{diag}(1, 1, -1, -1)$ . Therefore, for specular reflections, the intensity is maximized when  
 112  $a_{k,0} = g_{k,0}$ ,  $a_{k,1} = g_{k,1}$ ,  $a_{k,2} = -g_{k,2}$ , and  $a_{k,3} = -g_{k,3}$  (we shall call this the co-polarized case)  
 113 and minimized when  $a_{k,0} = g_{k,0}$ ,  $a_{k,1} = -g_{k,1}$ ,  $a_{k,2} = g_{k,2}$ , and  $a_{k,3} = g_{k,3}$  (cross-polarized  
 114 case). Cross-polarized vectors can fully suppress specular reflections, but if  $\mathbf{W}$  is constructed only  
 115 by cross-polarized vectors, then  $\mathbf{W} \mathbf{W}^T$  becomes singular, making it impossible to calculate the  
 116 full MM. In such case, only combinations of certain MM elements can be accurately determined.

117 The full MM measurement requires using angular sets that involve polarization states not  
 118 strictly co-polarized or cross-polarized, but also cases in between. Optimal angles can be

119 determined using optimization algorithms that maximize the area covered on the Poincaré sphere,  
 120 with the condition number serving as a merit function:

$$\kappa(\mathbf{W}) = \|\mathbf{W}\| \cdot \|\mathbf{W}^+\| \quad (9)$$

121 with  $\|\mathbf{W}\|$ ,  $\|\mathbf{W}^+\|$  being the 2-norm of the matrices  $\mathbf{W}$  and  $\mathbf{W}^+$  respectively.

122 Polarimetric optimization typically focuses on determining PSG and PSA parameters that  
 123 minimize the condition number. However, in this work, we also consider the minimization of  
 124 specular reflections in the optimization. Specifically, we aim to determine the angles  $\theta_0$  (PSG)  
 125 and  $\theta_1$  (PSA) that reduce the specular intensity  $\mathbf{I}$  in Eq. (7), while simultaneously keeping  $\kappa(\mathbf{W})$   
 126 as low as possible. Reducing specular reflections generally increases the condition number,  
 127 requiring a trade-off to balance these competing factors. Several angular sets (with  $N = 16$ ) were  
 128 computed by solving a global optimization problem using the differential evolution method. We  
 129 labeled these sets as A, B, C, D, E, and F, where set A corresponds to the lowest condition number  
 130 (without considering specular intensity in the optimization) and set F represents the greatest  
 131 suppression of specular intensity (that also leads to the highest condition number). Details of  
 132 the optimized angles are provided in the supporting information, including six sets of angles  
 133 optimized for our system.

134 Table 1 lists the condition number, maximum intensity, and mean intensity (averaged over  
 135 the 16 angles) for each angular set. These values correspond to our experimental setup, where  
 136 both compensators exhibit a retardance of approximately  $141^\circ$ . For different retardance values,  
 137 the angular sets will produce different intensities. The intensities are normalized so that the  
 138 maximum value is 1, occurring when the illumination and analyzed states are fully collinear after  
 139 specular reflection. Notably, the angular set with the lowest condition number (set A) corresponds  
 140 to an intensity near its maximum, while the set with the lowest specular intensity (set F) has  
 141 the highest condition number. Note that, for example, sets B and C already demonstrate that a  
 142 substantial decrease of the specular intensity is possible without compromising too much the  
 143 condition number.

144 The condition number is an algebraic metric that evaluates the numerical robustness of  
 145 polarimetric data inversion. However, it does not account for other factors that influence the  
 146 quality of polarimetric measurements, such as light intensity levels or the use of proper camera  
 147 exposure settings to fully utilize the dynamic range. For instance, if illumination and exposure  
 148 conditions are optimized for dataset A, measurements using datasets B, C, D, E, and F under  
 149 the same illumination/exposure settings will appear progressively darker and noisier compared  
 150 to A. This is due to reduced mean intensity and poorer polarimetric conditioning. In contrast,  
 151 if the illumination intensity or camera exposure is adjusted for each dataset to achieve roughly  
 152 the same mean intensity across all images, the performance differences between datasets may  
 153 change. This effect will be experimentally investigated in the following sections.

### 154 3. Experimental setup

155 The instrument used in the experiments reported utilizes a backscattering configuration, where  
 156 light is reflected from the sample at a very small angle of incidence. This is advantageous for  
 157 MM imaging as it eliminates the need for a beam-splitter used in systems where forward and  
 158 backward light share the same optical path, significantly simplifying the calibration process. The  
 159 backscattering configuration is also well-suited for biomedical wide-field imaging, where the  
 160 imaging optics elements are positioned at a considerable distance from the sample, enabling  
 161 the examination of a wider sample area. The imaging objective (a 16 mm fixed focal length  
 162 camera objective Thorlabs MVL16M23) is positioned outside the region between the Polarizer-  
 163 Sample-Analyzer components. The camera used is FLIR Grasshopper3 (GS3-U3-32S4M-C)  
 164 with a 12-bit ADC and a maximum resolution of  $2448 \times 2048$  pixels.



Angular set	Condition Number	Max. Intensity	Mean Intensity
A	5.07	0.92	0.48
B	5.64	0.71	0.42
C	9.69	0.40	0.25
D	14.87	0.28	0.16
E	30.65	0.22	0.12
F	42.25	0.18	0.11

Table 1. Values of condition number and intensity of the different angle sets for a retardance value of  $141^\circ$ . Intensity values have been normalized to their maximum value 1.

In our system, the polarization-state generator (PSG) and polarization-state analyzer (PSA) are composed of a compensator (Edmund Optics WP280 retarder) and a polarizer (Edmund Optics NIR linear polarizing film). The polarizers in the PSG and PSA are positioned in a crossed configuration, while both compensators are mounted on rotating motors (Thorlabs ELL14K) that rotate the retarders to achieve 16 different angular positions for each. We have used different collections of angles calculated as described in the previous section in order to decrease the amount of specular intensity while trying to obtain the least condition number possible. A calibration process is also required and was executed employing a specular reflecting mirror as a representative sample (which can be assumed to have MM diag(1, 1, -1, -1)) and using a non-linear least squares fitting algorithm that finds the retardance and offset angles values to obtain the best fit to this matrix. Measurements with all angular sets used the same calibration values. All measurements have been performed using a 660 nm LED as light source. At this wavelength, the retarders used have a retardance of  $141^\circ$  that is relatively close to the optimal value ( $132^\circ$  [27]) for polarimetric imaging .

#### 4. Results and analysis

Six consecutive MM measurements were performed on the same sample using the six distinct sets of angular configurations. The objective was to compare results from set A, optimized for the best condition number, with five other configurations designed to progressively reduce the intensity of specular reflections reaching the detector. To ensure comparability, the LED intensity was adjusted for each set so that the mean detector intensity remained approximately constant when using the different sets, i.e. trying to optimize the illumination condition for each angular set.

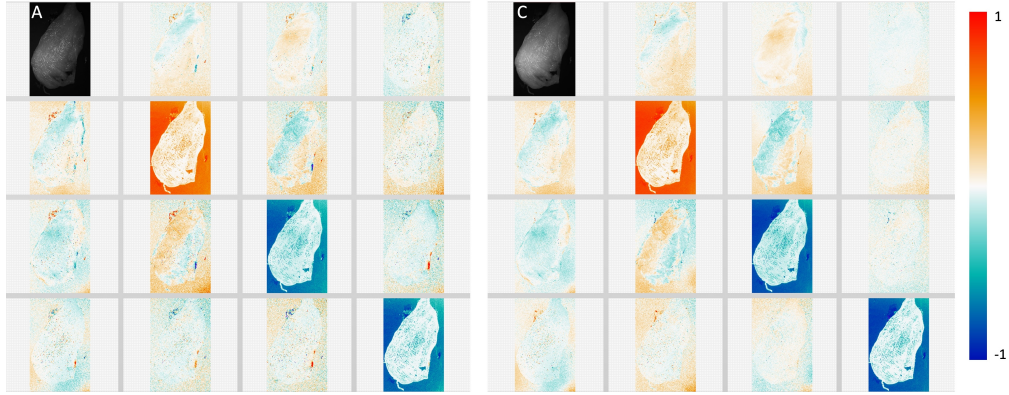


Fig. 1. Normalized Mueller matrices obtained using angular sets A and C. Off-diagonal elements are multiplied by a factor of 5 to enhance the visualization of the results. The  $m_{00}$  element has been replaced by the intensity image.

187 The experiments were carried out on various chicken breast samples purchased from a local  
 188 supermarket, all of which exhibited consistent trends. All the reported images have a resolution  
 189 of  $830 \times 1280$  pixels, which corresponds to an area of  $11.75 \times 18.15 \text{ cm}^2$ . For clarity, this section  
 190 focuses on the results obtained from a representative sample. Figure 1 displays the measured  
 191 MMs for angular sets A and C. To improve visualization, all off-diagonal elements are multiplied  
 192 by a factor of 5, as these elements are typically small in biological tissues due to significant  
 193 depolarization effects. Larger views of all 6 experimental MMs are available in the supplemental  
 194 document.

195 Fig. 2 shows the comparison between the different angular sets for the mean intensity (i.e. the  
 196  $m_{00}$  images that correspond to imaging with unpolarized light) and the depolarization index [28]  
 197 calculated from the MM. A clear variation in the intensity images is observed across the angular  
 198 sets, with specular highlights on the chicken breast surface progressively diminishing, leading to  
 199 improved tissue visualization. In contrast, the depolarization index images show no significant  
 200 variation between the sets, consistently indicating high depolarization levels (low depolarization  
 201 index) in the tissue.

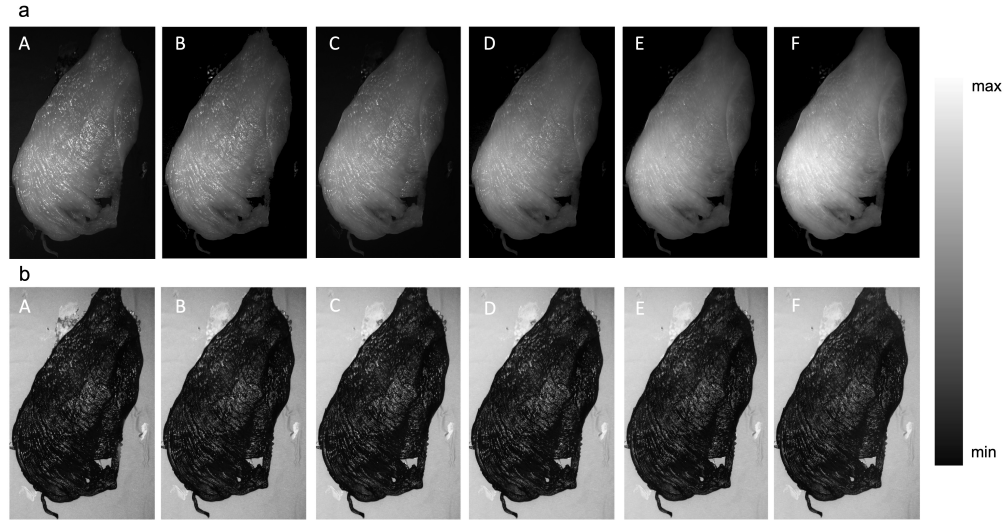


Fig. 2. Comparison of the intensity and depolarization index for the different angle sets. The color bar for images in a) ranges from 0 to 2000, and for images in b), from 0 to 1.

202 The measured MMs were analyzed using the differential Mueller matrix formalism [29], where  
 203 the differential matrix  $\mathbf{L}$  is obtained as  $\mathbf{L} = \ln \mathbf{M}$ . To ensure the matrix logarithm is well-defined  
 204 in backscattering configurations, the experimental MM  $\mathbf{M}$  is pre-processed by left-multiplying  
 205 it with  $\text{diag}(1, 1, -1, -1)$ , as outlined in [30]. This adjustment aligns the matrix format with  
 206 that of transmission measurements, allowing for straightforward computation using modern  
 207 numerical algorithms. Figs. 3 and 4 present the linear retardation and linear diattenuation values  
 208 obtained from the differential analysis, shown in terms of their magnitudes and orientation angles.  
 209 Diattenuation and not retardation is the main effect (besides depolarization) that can be measured  
 210 in chicken breast tissue at the NIR, despite the intrinsic birefringence of the fibrous breast tissue  
 211 that could be assessed in transmission measurements from histological cuts. In the NIR the breast  
 212 tissue has almost no absorption and the measured light in backscattering primarily originates  
 213 from shallow surface layers of the chicken breast tissue, where polarization-dependent scattering  
 214 leads to measurable diattenuation, affected by the polarization-dependent scattering properties  
 215 of the surface microstructure. Retardation is averaged out because the fibrous structures in the  
 216 chicken breast tissue are not uniformly aligned at the surface or within the shallow subsurface  
 217 layers.

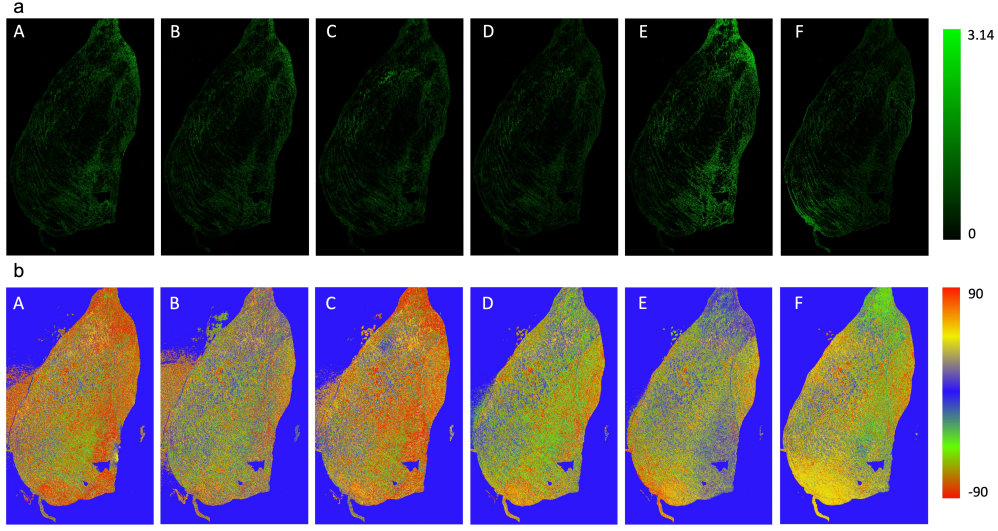


Fig. 3. Comparison of the magnitude and orientation of the linear retardation for the different angle sets.

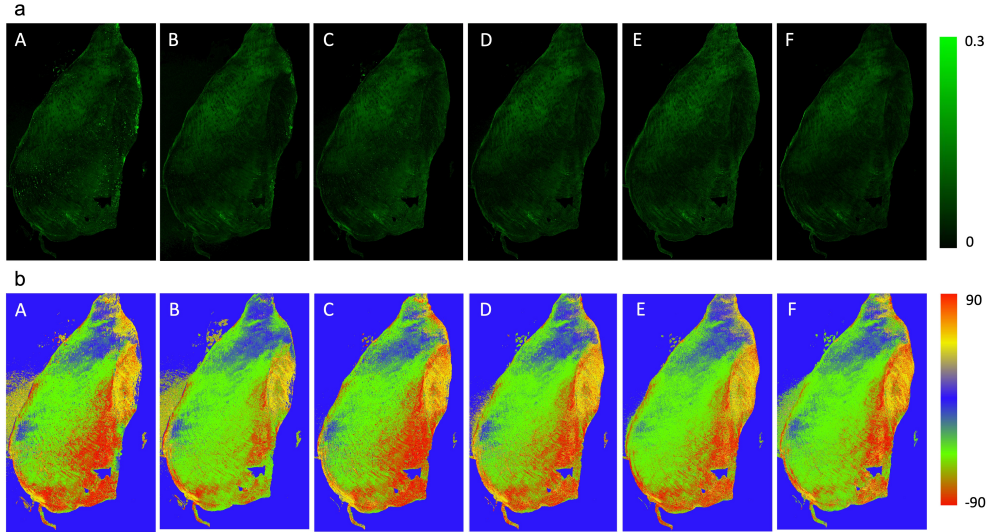


Fig. 4. Comparison of the magnitude and orientation of the diattenuation for the different angle sets.

218 Comparison between the different angular sets in Fig. 3 and 4 reveals that all measurements  
 219 appear to be relatively similar, indicating that despite the larger condition number of angular sets  
 220 B, C, D, E, and F with respect to A, there seems to be no clear advantage of dataset A with respect  
 221 to the others. It is worth emphasizing that while the angular sets progressively suppress specular  
 222 reflections and significantly enhance the visualization of the tissue through the  $m_{00}$  element,  
 223 they do not alter the measured polarimetric properties. This is evident from the six normalized  
 224 MMs provided in the supplemental document, which consistently show the same (or very similar)  
 225 values for the normalized MM elements across all angular sets. In other words, our method can

improve the tissue visualization but it does not change the measured polarization-depending parameters.

To complement visual inspection, image quality was quantitatively assessed using the Perception-based Image Quality Evaluator (PIQE) [31]. PIQE is an opinion-unaware and unsupervised metric that evaluates image quality without the need for a trained model. It measures block-wise distortion and computes the local variance of perceptibly distorted blocks to derive a quality score. A lower PIQE score indicates better image quality, with 0 representing an ideal image. Table 2 shows the PIQE values for intensity and the magnitude and orientation of the linear diattenuation of the different angle sets. Intensity image PIQE values decrease when advancing the angular set letter, PIQE values for the diattenuation images stay roughly on the same levels regardless of the chosen angular set.

Angular set	Intensity	Linear diattenuation (magnitude)	Linear diattenuation (orientation)
A	43.62	39.25	64.97
B	42.23	46.06	60.75
C	39.05	45.44	64.66
D	31.77	50.11	68.23
E	28.76	53.39	66.96
F	27.72	48.05	65.88

Table 2. PIQE values for intensity and the magnitude and orientation of the linear diattenuation of the different angle sets.

## 5. Conclusion

This work presents a novel method for reducing specular reflections in MM polarimetry by optimizing the angular configurations of the polarization state generator (PSG) and analyzer (PSA). By employing near-cross-polarized states, the proposed approach effectively suppresses specular highlights while preserving depolarized signals from biological tissues. Experimental results on chicken breast samples demonstrate that this method significantly improves tissue visualization and preserves the quality of polarimetric imaging.

The optimization of angular sets is made by searching a trade-off between minimizing specular reflections and maintaining favorable polarimetric conditioning, as quantified by the condition number. While the angular set with the lowest possible condition number ensures better numerical robustness, configurations also designed to reduce specular intensity provide improved imaging contrast and reduced specular artifacts. Quantitative evaluation using the PIQE metric further validates the enhanced quality of intensity images and preservation and diattenuation images achieved with the optimized configurations.

This study emphasizes the importance of balancing illumination conditions, polarimetric conditioning, and specular reflection suppression in imaging systems. The proposed methodology enhances the applicability of MM polarimetry in challenging conditions such as in-situ biomedical imaging and provides a foundation for extending its use to other scattering media. Future research will focus on adapting this approach to dynamic imaging scenarios and exploring its applicability across different wavelength ranges, broadening its potential for advanced optical diagnostics and material characterization.

258 **Funding** Ministerio de Ciencia e Innovación of Spain (TED2021-129639B-I00, CNS2022-  
259 136051 and PID2022-138699OB-I00)

260 **Disclosures** The authors declare no conflicts of interest.

## 261 References

- 262 1. J. Chue-Sang, N. Holness, M. Gonzalez, *et al.*, "Use of mueller matrix colposcopy in the characterization of cervical  
263 collagen anisotropy," *J. biomedical optics* **23**, 121605–121605 (2018).
- 264 2. H. He, R. Liao, N. Zeng, *et al.*, "Mueller matrix polarimetry—an emerging new tool for characterizing the  
265 microstructural feature of complex biological specimen," *J. Light. Technol.* **37**, 2534–2548 (2018).
- 266 3. G. Yao and L. V. Wang, "Two-dimensional depth-resolved mueller matrix characterization of biological tissue by  
267 optical coherence tomography," *Opt. Lett.* **24**, 537–539 (1999).
- 268 4. S. Alali and A. Vitkin, "Polarized light imaging in biomedicine: emerging mueller matrix methodologies for bulk  
269 tissue assessment," *J. biomedical optics* **20**, 061104–061104 (2015).
- 270 5. O. Angelsky, Y. Y. Tomka, A. Ushenko, *et al.*, "Investigation of 2d mueller matrix structure of biological tissues for  
271 pre-clinical diagnostics of their pathological states," *J. Phys. D: Appl. Phys.* **38**, 4227 (2005).
- 272 6. J. Qi and D. S. Elson, "Mueller polarimetric imaging for surgical and diagnostic applications: a review," *J.*  
273 *biophotonics* **10**, 950–982 (2017).
- 274 7. I. Pardo, S. Bian, J. Gomis-Brescó, *et al.*, "Wide-field mueller matrix polarimetry for spectral characterization of  
275 basic biological tissues: Muscle, fat, connective tissue, and skin," *J. Biophotonics* **17**, e202300252 (2024).
- 276 8. P. Sampaio, M. Lopez-Antuña, F. Storni, *et al.*, "Müller matrix polarimetry for pancreatic tissue characterization,"  
277 *Sci. Reports* **13**, 16417 (2023).
- 278 9. M. Menzel, M. Axer, K. Amunts, *et al.*, "Diattenuation imaging reveals different brain tissue properties," *Sci. reports*  
279 **9**, 1939 (2019).
- 280 10. M. Dubreuil, F. Tissier, S. Rivet, and Y. L. Grand, "Linear diattenuation imaging of biological tissues with near  
281 infrared mueller scanning microscopy," *Biomed. optics express* **12**, 41–54 (2020).
- 282 11. H. Li, I. Pardo, and O. Arteaga, "Underwater mueller matrix de-scattering imaging under the influence of natural  
283 light," *Opt. Lasers Eng.* Submitted (2024).
- 284 12. J. Chue-Sang, Y. Bai, S. Stoff, *et al.*, "Use of mueller matrix polarimetry and optical coherence tomography in the  
285 characterization of cervical collagen anisotropy," *J. biomedical optics* **22**, 086010–086010 (2017).
- 286 13. B. Chen, W. Li, H. He, *et al.*, "Analysis and calibration of linear birefringence orientation parameters derived from  
287 mueller matrix for multi-layered tissues," *Opt. Lasers Eng.* **146**, 106690 (2021).
- 288 14. X. Cheng, Y. Li, J. Mertz, *et al.*, "Development of a beam propagation method to simulate the point spread function  
289 degradation in scattering media," *Opt. Lett.* **44**, 4989–4992 (2019).
- 290 15. I. Estévez, F. Oliveira, P. Braga-Fernandes, *et al.*, "Urban objects classification using mueller matrix polarimetry and  
291 machine learning," *Opt. express* **30**, 28385–28400 (2022).
- 292 16. M. Amir Sohail, C. Ghosh, S. Mandal, and M. Maruf Mallick, *Specular Reflection Removal Techniques for Noisy and*  
293 *Non-ideal Iris Images: Two New Approaches* (Springer Nature Singapore, 2022), p. 277–289.
- 294 17. A. Anwer, S. Ainouz, N. M. Saad, *et al.*, "Joint network for specular highlight detection and adversarial generation of  
295 specular-free images trained with polarimetric data," *Neurocomputing* **559**, 126769 (2023).
- 296 18. W. Xia, E. C. Chen, S. E. Pautler, and T. M. Peters, "A global optimization method for specular highlight removal  
297 from a single image," *IEEE Access* **7**, 125976–125990 (2019).
- 298 19. M. Arnold, A. Ghosh, S. Ameling, and G. Lacey, "Automatic segmentation and inpainting of specular highlights for  
299 endoscopic imaging," *EURASIP J. on Image Video Process.* **2010**, 1–12 (2010).
- 300 20. P. Schucht, H. R. Lee, H. M. Mezouar, *et al.*, "Visualization of white matter fiber tracts of brain tissue sections with  
301 wide-field imaging mueller polarimetry," *IEEE transactions on medical imaging* **39**, 4376–4382 (2020).
- 302 21. W. Jiao, Z. Zhang, N. Zeng, *et al.*, "Complex spatial illumination scheme optimization of backscattering mueller  
303 matrix polarimetry for tissue imaging and biosensing," *Biosensors* **14**, 208 (2024).
- 304 22. L. Wang and D. Zimnyakov, *Optical polarization in biomedical applications*, vol. 467 (Springer, 2006).
- 305 23. S. Gioux, A. Mazhar, and D. J. Cuccia, "Spatial frequency domain imaging in 2019: principles, applications, and  
306 perspectives," *J. biomedical optics* **24**, 071613–071613 (2019).
- 307 24. S. L. Jacques, J. C. Ramella-Roman, and K. Lee, "Imaging skin pathology with polarized light," *J. biomedical optics*  
308 **7**, 329–340 (2002).
- 309 25. D. W. Paul, P. Ghassemi, J. C. Ramella-Roman, *et al.*, "Noninvasive imaging technologies for cutaneous wound  
310 assessment: A review," *Wound Repair Regen.* **23**, 149–162 (2015).
- 311 26. R. A. Chipman, W.-S. T. Lam, and G. Young, *Polarized Light and Optical Systems* (CRC Press, 2018).
- 312 27. O. Arteaga and S. Bian, "Mueller matrix imaging," *Opt. Polarim. Modalities for Biomed. Res.* pp. 77–99 (2023).
- 313 28. J. Gil and E. Bernabeu, "Depolarization and polarization indices of an optical system," *J. Mod. Opt. - J MOD OPTIC*  
314 **33**, 185–189 (1986).
- 315 29. O. Arteaga, "Historical revision of the differential stokes–mueller formalism: discussion," *J. Opt. Soc. Am. A* **34**,  
316 410–414 (2017).

- 317 30. O. Arteaga and R. Ossikovski, “Mueller matrix analysis, decompositions and novel quantitative approaches to data  
318 analysis,” in *Polarized Light in Biomedical Imaging and Sensing*, (Springer, 2023), chap. 5.
- 319 31. R. W. Chan and P. B. Goldsmith, “A psychovisually-based image quality evaluator for jpeg images,” in *Smc 2000*  
320 *conference proceedings. 2000 ieee international conference on systems, man and cybernetics.* ‘cybernetics evolving to  
321 *systems, humans, organizations, and their complex interactions*’(cat. no. 0, vol. 2 (IEEE, 2000), pp. 1541–1546.